

A *Chandra* Search for Coronal X Rays from the Cool White Dwarf GD 356

Martin C. Weisskopf¹, Kinwah Wu², Virginia Trimble^{3,4}, Stephen L. O'Dell⁵,
Ronald F. Elsner⁵, Vyacheslav E. Zavlin^{5,6}, and Chryssa Kouveliotou⁵

ABSTRACT

We report observations with the *Chandra* X-ray Observatory of the single, cool, magnetic white dwarf GD 356. For consistent comparison with other X-ray observations of single white dwarfs, we also re-analyzed archival *ROSAT* data for GD 356 (GJ 1205), G 99-47 (GR 290 = V1201 Ori), GD 90, G 195-19 (EG250 = GJ 339.1), and WD 2316+123 and archival *Chandra* data for LHS 1038 (GJ 1004) and GD 358 (V777 Her). Our *Chandra* observation detected no X rays from GD 356, setting the most restrictive upper limit to the X-ray luminosity from any cool white dwarf — $L_X < 6.0 \times 10^{25}$ erg s⁻¹, at 99.7% confidence, for a 1-keV thermal-bremsstrahlung spectrum. The corresponding limit to the electron density is $n_0 < 4.4 \times 10^{11}$ cm⁻³. Our re-analysis of the archival data confirmed the non-detections reported by the original investigators. We discuss the implications of our and prior observations on models for coronal emission from white dwarfs. For magnetic white dwarfs, we emphasize the more stringent constraints imposed by cyclotron radiation. In addition, we describe (in an appendix) a statistical methodology for detecting a source and for constraining the strength of a source, which applies even when the number of source or background events is small.

Subject headings: X rays: individual (GD 356) — white dwarfs — stars: corone — radiation mechanisms: thermal — methods: statistical

¹NASA Marshall Space Flight Center, VP60, Huntsville, AL 35812 (martin@smoker.msfc.nasa.gov)

²Mullard Space Science Laboratory, University College London, Holmbury St. Mary, Surrey RH5 6NT, UK

³Dept. of Physics and Astronomy, University of California, Irvine, CA 92697-4575

⁴Las Cumbres Observatory, Goleta, CA 93117

⁵NASA Marshall Space Flight Center, VP62, Huntsville, AL 35812

⁶Research Fellow, NASA Postdoctoral Program (NPP)

1. Introduction

Several theorists (e.g., Zheleznyakov & Litvinchuk 1984; Serber 1990; Thomas, Markiel, & Van Horn 1995) have suggested that single, cool, magnetic white dwarfs might have coronae. Some observers (Fontaine, Montmerle, & Michaud 1982; Arnaud et al. 1992; Cavallo, Arnaud, & Trimble 1993; Musielak, Porter, & Davis 1995; Musielak et al. 2003) have previously searched for X radiation that might be emitted by hot gas above a white-dwarf photosphere. There were no persuasive detections, despite one false alarm — GR 290, in archival Einstein data (Arnaud et al. 1992). We here report another upper limit, more stringent than the previous ones, for the white-dwarf star GD 356.

Three considerations motivated these X-ray searches: (a) the preponderance of magnetic white dwarfs among the X-ray emitting cataclysmic variables; (b) the possibility that some features in the optical spectra of magnetic white dwarfs might be cyclotron resonances (Zheleznyakov & Litvinchuk 1984); and (c) the feeling that coronal heating is not so well understood that constraints from other kinds of stars wouldn't be worthwhile. In the special case of GD 356, the presence of Balmer lines in emission imply at least a chromosphere, making more plausible the existence of a corona. Magnetic fields in most of the stars examined so far (including GD 356) are 1 MG or more, thought to be fossils from the white dwarfs' previous lives as Ap stars. More recent measurements of variable, weaker fields in some white dwarfs — the DBV GD 358 (Winget et al. 1994) and the DA LHS 1038 (Schmidt & Smith 1995) — suggest non-fossil magnetism. Calculations (Thomas, Markiel, & Van Horn 1995) indicate that cool white dwarfs with convective envelopes can support α - ω dynamos capable of generating 100-kG fields.

Section 2 reviews recent theoretical considerations; Section 3, limits from previous searches. Next, Section 4 presents the results of our *Chandra* observations of GD 356; Section 5, our re-analysis of prior *ROSAT* and *Chandra* observations of GD 356 and of other white dwarfs. Finally, Section 6 discusses the implications of the new and re-analyzed results and emphasizes the importance of thermal cyclotron radiation in magnetic white dwarfs (cf. Zheleznyakov, Koryagin, & Serber 2004, and references therein).

2. Magnetic coronal activity from white dwarfs with a convective layer

White dwarfs are the class of compact objects that we presumably understand best. Nevertheless, several fundamental issues remain unresolved. For instance, are white-dwarf magnetic fields all relic (fossil) or are there transient field components generated by dynamos? What excites the mysterious line emission from some white dwarfs? Are X rays from white

dwarfs, when detected, simply thermal emission from a deep photosphere?

All stars show a certain degree of magnetism. Quite often, coronal activity in non-degenerate stars demonstrates the presence of a magnetic field, presumably produced via magnetohydrodynamic (MHD) processes. In the canonical model, an α - ω dynamo in a convective stellar envelope generates the field; acoustic waves emerging from deep beneath the stellar atmosphere heat the corona. In contrast, the magnetic fields of degenerate stars — such as white dwarfs — may be fossil fields. Such a fossil field, together with a small, static atmospheric scale height, would lead one to conclude that white dwarfs should not have coronae. However, some studies have challenged this conclusion. For example, theoretical arguments (Wesmael et al. 1980; Koester 2002) suggest that the cooler ($T_{\text{eff}} < 18,000$ K) DA white dwarfs and ($T_{\text{eff}} < 30,000$ K) DB white dwarfs could possess a convective zone — a necessary ingredient for coronal X-ray emission. Further, differential rotation, if it occurs in white dwarfs (cf. Kawaler, Sekii, & Gough 1999), might support a magnetic dynamo. As noted above, the magnetic-field strength generated by an α - ω dynamo in a cool white dwarf might approach 100 kG (Thomas, Markiel, & Van Horn 1995).

Most important is the presence of emission lines from some white dwarfs with no detectable companion. Among these, and thus especially interesting, are the H-Balmer line emission from the nearby (21.1 pc) white dwarf GD 356 (Greenstein & McCarthy 1985) and the metal lines from G227-5 and from G35-26 (Provencal, Shipman, & MacDonald 2005). For single white dwarfs, such emission lines indicate some chromospheric activity. Alternative models for the H emission lines in GD 356 include accretion of the interstellar medium and the presence of an interacting companion star or even a planet (Greenstein & McCarthy 1985; Li, Wickramasinghe, & Ferrario 1998). The estimated luminosity of the Zeeman-split H α emission lines of GD 356 is $\approx 2.1 \times 10^{27}$ erg s $^{-1}$. Further, the flat Balmer decrement ($f(\text{H}\alpha)/f(\text{H}\beta) \approx 1.2$, Greenstein & McCarthy 1985) excludes photo-ionization and recombination in an optically thin gas, suggesting instead a dense emission region with electron number density $n_e \approx 10^{14}$ cm $^{-3}$ (Greenstein & McCarthy 1985). A possible cause of the chromospheric Balmer line emission is irradiation by UV/X rays from a hot magnetic corona above the cooler white-dwarf atmosphere. The presence of a white-dwarf magnetic corona remains unverified, which motivated our *Chandra* observation. However, reported temporal variations of the magnetic field of (DBV) GD 358 (Winget et al. 1994) and of (DA) LHS 1038 (Schmidt & Smith 1995) are consistent with a magnetic corona.

In addition to facilitating the MHD dynamo process, a convective zone (Böhm & Cassinelli 1971) also results in acoustic-wave generation. Calculations show that the flux of such acoustic waves can be as large as $\approx 10^{10}$ erg cm $^{-2}$ s $^{-1}$ (Musielak 1987). If the acoustic energy reaches the white-dwarf surface unabsorbed, it can provide a total luminosity

$\approx 5 \times 10^{28}$ erg s⁻¹. However, due to radiative damping and wave trapping, a substantial fraction of this acoustic energy will not reach the white-dwarf atmosphere. For cool DA and DB white dwarfs with sensible parameters, fast-mode acoustic waves would attenuate to a negligible level at the white-dwarf atmosphere (Musielak 1987), thus failing to power a magnetic corona. Instead, wave trapping excites p-mode stellar pulsations (Musielak & Fontenla 1989). In contrast, if the white dwarf is magnetic (but not so much as to suppress convection), transverse slow modes can propagate, carrying perhaps 60%–80% (Musielak 1987) of the wave energy into the stellar atmosphere.

3. Previous X-ray observations

The detection of X radiation from Sirius B (Mewe et al. 1975) established that white dwarfs are soft-X-ray sources. Subsequent *Einstein*, *EXOSAT* and *ROSAT* observations (e.g., Musielak 1987; Kahn et al. 1984; Petre, Shipman, & Canizares 1986; Paerels & Heise 1989; Koester et al. 1990; Kidder et al. 1992; Barstow, et al. 1993) detected X radiation from a number of hot ($T_{\text{eff}} > 30,000$ K) white dwarfs. Thermal emission from the photosphere (Shipman 1976) accounts for the X-ray emission in all but one case: For the (DO) KPD 0005+5106, optically thin thermal emission better fits the observed *ROSAT* data (Fleming, Werner, & Barstow 1993), indicating a hot tenuous plasma layer enveloping the white dwarf. For KPD 0005+5106, the inferred temperature of the X-ray emitting plasma is 0.2–0.3 MK, lower than the typical temperature of magnetic coronae around late-type stars and perhaps indicating a hot wind resembling those of O/B stars.

Searches, with *Einstein* and *EXOSAT* (Fontaine, Montmerle, & Michaud 1982; Arnaud et al. 1992) and with *ROSAT* (Cavallo, Arnaud, & Trimble 1993; Musielak, Porter, & Davis 1995), for coronal X rays from cool white dwarfs yielded no firm detections. For searches with the *ROSAT* Position-Sensitive Proportional Counter (PSPC), Cavallo, Arnaud, & Trimble (1993) established X-ray upper limits for the white dwarfs G 99-47 and G 195-19; Musielak, Porter, & Davis (1995), for GD 90, GD 356, and WD 2316+123. Likewise, observations (Musielak et al. 2003) with the *Chandra* Advanced CCD Imaging Spectrometer (ACIS) of reportedly magnetically-varying white dwarfs, detected X radiation neither from LHS 1038 nor from GD 358. Table 1 summarizes some relevant general properties of these white dwarfs: Column 1 gives the name; columns 2 and 3, the epoch-2000 right ascension RA(J2000) and declination Dec(J2000); columns 4 and 5, the proper-motion components; column 6, the distance; column 7, the spectral type; and columns 8 and 9, the surface effective temperature and magnetic field.

The previous searches determined upper limits to the X-ray luminosity for a thermal-

bremsstrahlung spectrum with negligible interstellar absorption. Assuming a coronal temperature of 11.6 MK (1.0 keV), Cavallo, Arnaud, & Trimble (1993) obtained *ROSAT*-PSPC 99%-confidence limits to the 0.1–2.5-keV luminosity of $< 2.9 \times 10^{26}$ erg s $^{-1}$ for G 99-47 and $< 1.4 \times 10^{26}$ erg s $^{-1}$ for G 195-19. Assuming a coronal temperature of 2.5 MK (0.215 keV), Musielak, Porter, & Davis (1995) obtained *ROSAT*-PSPC 99.7%-confidence (3- σ) limits to the 0.1–2.4-keV luminosity of $< 7.8 \times 10^{27}$ erg s $^{-1}$ for GD 90, $< 4.4 \times 10^{26}$ erg s $^{-1}$ for GD 356, and $< 3.4 \times 10^{27}$ erg s $^{-1}$ for WD 2316+123. Under the same assumptions but using *Chandra*-ACIS observations, Musielak et al. (2003) found $< 4.3 \times 10^{26}$ erg s $^{-1}$ for LHS 1038 and $< 4.3 \times 10^{27}$ erg s $^{-1}$ for GD 358. These upper limits were comparable to the X-ray luminosities that Musielak et al. (2003) had predicted for LHS 1038 and GD 358 — 5×10^{26} erg s $^{-1}$ and 5×10^{27} erg s $^{-1}$, respectively. For uniform comparison of results over a wider range of assumed parameters, we re-analyzed (§5 and Table 2) the relevant archived *Chandra* (§5.1) and *ROSAT* (§5.2) data.

4. The *Chandra* observation of GD 356

We obtained a 31.8-ks *Chandra* observation (ObsID 4484, 2005 May 24) using the Advanced CCD Imaging Spectrometer (ACIS) S3 (back-illuminated) CCD in the faint, timed-exposure mode, with 3.141-s frame time. Background levels were nominal throughout the observation. Standard *Chandra* X-ray Center (CXC) processing (ASCDS version number CIAO3.2) provided level-2 event files. In analyzing data, we utilized events in pulse-invariant channels corresponding to 0.5 to 8.0 keV.

Our *Chandra* observation found no X rays in a 1''-radius detect cell at the epoch-2005.39 position of GD 356 — 16^h 40^m 57^s.23 +53° 41' 8".6, after adjustment of the epoch-2000 coordinates for proper motion (Table 1). The nearest detected X-ray source — #6 in Table 3 — lies 46'' from GD 356. To determine the background, we “punched out” the detected X-ray sources eliminating all counts within a 20- σ radius of each position in Table 3. Table 2 summarizes the results for our *Chandra* observation of GD 356, as well as for our re-analysis (§5) of previous *Chandra* (§5.1) and *ROSAT* (§5.2) searches for X-ray emission from this and other single white dwarfs. Column 1 lists the name of the white dwarf; column 2, the observatory used; column 3, the epoch relative to 2000.00 (used to adjust for proper motion); and column 4, the integration time. Column 5 presents the number of detected counts m_T in the “Target” (detect) cell T and column 6, its solid angle Ω_T . Analogously, column 7 presents the number of detected counts m_R in the “Reference” region R and column 8, its solid angle Ω_R . Finally, columns 9, 10, 11, and 12 list the confidence level for detection of a source (§A.2), the 99.7%-confidence upper limit on the expectation value of the

number of source counts (§A.3), and the corresponding limits on the X-ray luminosity (for a 1-keV thermal-bremsstrahlung spectrum) and on the electron density, which follow from the analysis below. Owing to the very small (1-'' radius) detect cell afforded by *Chandra*'s sub-arcsecond resolution, only two (2) counts in the Target aperture would have constituted a (3- σ) 99.7%-confidence detection for either of the three *Chandra* data sets! Neither of the three *Chandra* observations found an event in the detect cell.

A statistical analysis (Appendix A) of the data yields (Equation A8) the confidence level for detection of a source within the Target (detect) cell and (Equation A22) a 99.7%-confidence upper limit to the expected number of source counts in the Target (detection) cell T . Before converting the source counts to a flux and luminosity, we correct for the fraction of the point spread function (PSF) outside the detect cell. For *Chandra* and almost any soft spectrum, about 90%¹ of the source photons for an on-axis source would lie within the chosen detect cell. To convert the resulting 5-count (4.5/0.9) limit to a flux, we calculated the redistribution matrix (rmf) and effective area (arf) functions appropriate to the location of GD 356 in the focal plane, using the *Chandra* CIAO 3.3 software tools `mkacisarmf` and `mkarf`, following the analysis thread² for creating these functions for a specific location. Assuming a column $N_H = 5 \times 10^{18} \text{ cm}^{-2}$ and a thermal bremsstrahlung spectrum, we used XSPEC (v11.3.2)³ with `abund` set to `wilm`, `xsect` set to `vern`, and `tbabs(bremss)` as the model. For each assumed value for the coronal temperature, we adjusted the model normalization until the absorbed flux produced 5.0 counts in the S3 detector in the observing time of the *Chandra* observation. Feeding this normalization into XSPEC, we used the `dummyrsp` feature to calculate the flux for 10^4 bins over the energy range 10^{-5} keV to 100 keV. We used this approach to improve the accuracy of our flux calculations since the instrument response is calculated over a more restricted energy range, and with cruder energy bins. We then calculated fluxes over the band from 0.01 to 100 keV, now setting the column density to zero to obtain the unabsorbed flux.

The upper panel of Figure 1 plots the 3- σ upper limit to the total luminosity, as a function of coronal temperature, for our observation of GD 356 and for our re-analysis (§5) of previous white-dwarf observations. The upper panel of Figure 2 shows the corresponding upper limit to the electron density for an effective emitting volume $4\pi R^2 H$ — appropriate for a geometrically thin ($H \ll R$), transparent, atmosphere of (exponential) scale height H around a sphere of radius R . For the ion density, we assume a fully ionized plasma of

¹see <http://asc.harvard.edu/proposer/POG/index.html>

²see <http://cxc.harvard.edu/ciao/ahelp/mkacisrmf.html>

³see <http://xspec.gsfc.nasa.gov/>

hydrogen and helium with $n_{\text{He}}/n_{\text{H}} = 0.1$, such that $\sum n_i Z_i^2 = 1.4 n_e$. The bremsstrahlung emissivity then goes as $1.4 \bar{n}_e^2 = 1.4 n_0^2/2$, where n_0 is the electron density at the base of an isothermal corona. Note that only about half the coronal emission emerges, due to photospheric absorption of most of the downward coronal flux. Using GD 356’s 21.1-pc parallax distance (van Altena, Lee, & Hoffleit 1995) and published UB V (Mermilliod & Mermilliod 1994) and JHK (Skrutskie et al. 2006) photometry, we obtain the photospheric temperature $T_s = 7840$ K and radius $R = 0.0105 R_{\odot} = 7.34 \times 10^8$ cm. For the coronal scale height, we use $H = (2 \times 10^7 \text{ cm}) kT/(1 \text{ keV})$, corresponding to a surface gravity $\log[g(\text{cgs})] = 8$. The lower panels of Figures 1 and 2 display analogous limits for the `tbabs(mekal)` Mewe–Kaastra–Liedahl (MEKAL) model with parameters as above, but `abund` set to `lodd`.

Besides examining the white-dwarf location for X rays, we searched for X-ray sources anywhere on S3 employing techniques described in Tennant (2006). For the 31.8-ks *Chandra* observation, Table 3 lists the X-ray properties of the 23 detected sources, each designated with a source number in column 1. Columns 2–5 give, respectively, right ascension RA(J2000), declination Dec(J2000), extraction radius θ_{ext} , and approximate number of X-ray counts m_D detected from the source. The single-axis RMS error in the X-ray-source position is $\sigma_X = [(\sigma_{\text{PSF}}^2/m_D) + \sigma_{\text{sys}}^2]^{1/2}$, where m_D is the approximate number of detected events above background, σ_{PSF} is the dispersion of the circular Gaussian that approximately matches the PSF at the source location, and σ_{sys} is a systematic error. Uncertainties in the plate scale⁴ imply $\sigma_{\text{sys}} \approx 0''.13$: To be conservative, we set $\sigma_{\text{sys}} = 0''.2$ (per axis). Column 6 gives the radial uncertainty $\theta_{99} = 3.03 \sigma_X$ in the X-ray position — i.e., $\chi_2^2 = 9.21 = 3.03^2$ corresponds to 99% confidence on 2 degrees of freedom, for inclusion of the true source position.

5. Re-analysis of previous observations.

For consistent comparison of X-ray observations, we also re-analyzed certain prior *Chandra* (§5.1) and *ROSAT* (§5.2) observations of single, cool white dwarfs. The *Chandra* observations used the ACIS-S instrument; the *ROSAT* observations, the PSPC.

5.1. Prior *Chandra* Observations

We re-processed and analyzed previous *Chandra* observations of the cool white dwarfs LHS 1038 (ObsID 1864, 5.88 ks) and GD 358 (ObsID 1865, 4.88 ks), in the same manner

⁴See <http://asc.harvard.edu/cal/hrma/optaxis/platescale/>

as for GD 356 (§4). Table 2 summarizes relevant parameters and results. Figure 1 shows the total luminosity ($3\text{-}\sigma$) 99.7%-confidence limits, for distances listed in Table 1. Figure 2 plots the corresponding upper limits to the electron density, approximating the radius of each white dwarf by that of GD 356 (§4).

As described above for our observation of the GD-356 field (§4), we also searched for X-ray sources in the S3 observations of the LHS-1038 and GD-358 fields. In the same form as Table 3, Tables 4 and 5 list X-ray sources detected on S3, for the LHS-1038 and GD-358 fields, respectively.

5.2. ROSAT Observations

Table 2 also summarizes our re-analysis of the *ROSAT*-PSPC observations, first analyzed by Cavallo, Arnaud, & Trimble (1993) and by Musielak, Porter, & Davis (1995). For the re-analysis, we selected the 0.1–2.4-keV energy band, a Target region of 1.5' (source extraction) radius, and an annular Reference region 1.5'–2.5' radius (for background estimation), as did Musielak, Porter, & Davis (1995). For sufficiently soft sources ($E < 0.5$ keV), most ($\geq 97\%$) of the flux from a source lies within the 1.5'-radius Target (detect) region (Boese 2000). Toward higher energies, the upper limits will be somewhat conservative because a decreasing fraction of source events appears in the Target aperture, while an increasing fraction appears in the Reference aperture. Furthermore, the *ROSAT* exposures are not sufficiently long to measure the background accurately. Appendix A describes a statistical methodology for dealing with these issues.

Following procedures described above (§4) but now using the *ROSAT*-PSPC response matrix, we established ($3\text{-}\sigma$) 99.7%-confidence upper limits to the expected number of source counts and then converted those to flux and luminosity. For calculating luminosity, we used the distances listed in Table 1. Figure 1 plots the derived luminosity limits as a function of assumed temperature for the bremsstrahlung (upper panel) and MEKAL (lower panel) spectral models. Figure 2 shows the corresponding $3\text{-}\sigma$ upper limits to the electron density, again approximating the radius of each white dwarf by that of GD 356 (§4).

6. Discussion

The objective of this investigation was to determine whether single, cool white dwarfs emit X radiation indicative of magnetic coronal activity. To assess the scientific implications of these null detections, we first (§6.1) discuss issues related to the formation of a magnetic

corona around a white dwarf. We then (§6.2) examine the rather severe constraints that cyclotron emission lines and radiative loss impose on a corona around a cool magnetic white dwarf, such as GD 356. Finally (§6.3), we summarize our results and conclusions about hypothesized hot coronae around magnetic white dwarfs.

6.1. Formation of a Corona

The existence of coronae around single, cool white dwarfs remains an unsettled issue: This, of course, motivated our search for X-ray evidence. Here we briefly address some questions relevant to the formation of a magnetic corona.

1. Is there a convection zone? Theoretical studies have indicated that convection can occur in white dwarfs for certain temperature ranges. Analyses of white-dwarf atmospheric elemental abundance also evidence convective activity. Thus, it is quite plausible that some white dwarfs possess a convection zone that generates acoustic waves.
2. How much acoustic wave energy is generated in the convection zone? Calculations (Musielak 1987; Winget et al. 1994) have shown that the convection-generated acoustic flux could exceed $10^8 \text{ erg cm}^{-2} \text{ s}^{-1}$ and may reach $10^{10} \text{ erg cm}^{-2} \text{ s}^{-1}$ for DA white dwarfs and $10^{11} \text{ erg cm}^{-2} \text{ s}^{-1}$ for DB white dwarfs.
3. What fraction of the acoustic wave energy is transmitted to the white-dwarf surface? For white dwarf with a substantial magnetic field ($B \approx 10^4 \text{ G}$ or higher), more than half of the wave energy generated in the convection zone can reach the white-dwarf atmosphere. If all the wave energy is converted into coronal X rays, the expected luminosity will be $\approx 10^{27} - 10^{30} \text{ erg s}^{-1}$. Our upper limit to the X-ray luminosity for GD 356 is an order of magnitude below $10^{27} \text{ erg s}^{-1}$ over most of the range of assumed temperatures. This implies either that the putative convection zone generates less acoustic energy, that the efficiency of acoustic-wave transmission to the surface is smaller, or that a corona fails to form even if the acoustic energy reaches the white-dwarf surface.
4. Can a magnetic corona form, given sufficient energy provided by the acoustic flux? The null detection of coronal X rays from white dwarfs has led some (see e.g., Musielak, Winget, & Montgomery 2005) to suggest that the emerging acoustic flux causes chromospheric activity rather than formation of a hot corona. An example of such chromospheric activity would be oscillations resulting from the stellar atmosphere to propagating acoustic waves in the presence of a temperature inversion (Musielak, Winget, &

Montgomery 2005). Whether acoustic waves generate chromospheric activity remains unverified. Nevertheless, a number of systems exhibit chromospheric activity. The luminosity of H α emission lines in GD 356 is $\approx 1.8 \times 10^{27}$ erg s $^{-1}$ (see Greenstein & McCarthy 1985). Our *Chandra* observation eliminates the possibility that irradiation of the atmosphere by coronal X rays powers the Balmer lines. Further, it is not clear that atmospheric oscillations can account for the luminosity of Balmer emission lines in GD 356.

While coronal X radiation from cool ($T_{\text{eff}} < 10,000$ K) magnetic white dwarfs remains undetected, X radiation from hot optically thin thermal plasmas appears to occur from very hot (1.2×10^5 K) white dwarf KPD 0005+5106. Now the question is this: Without a magnetic corona, what supports the hot plasma envelope in the strong gravitational field of the white dwarf? Radiation driven envelopes — predicted for hot white dwarfs (Bespalov & Zheleznyakov 1990; Zheleznyakov, Serber, & Kuijpers 1996) — could provide this support. Provided the white dwarf has a strong magnetic field, cyclotron-resonance radiation pressure from photospheric radiation could drive the wind, with an estimated mass-loss rate $\approx 2 \times 10^{10}$ g s $^{-1}$. Thus, a hot magnetic white dwarf could emit X rays from an optically thin, thermal plasma in a radiation-driven outflow.

6.2. Cyclotron Radiation

The *Chandra* observation sets stringent constraints on a supposed hot corona above the white-dwarf atmosphere. For GD 356, the X-ray luminosity $L_X < 6.0 \times 10^{25}$ erg s $^{-1}$ and electron number density $n_0 < 4.4 \times 10^{11}$ cm $^{-3}$ at the base of a corona of (exponential) scale height of 2.0×10^7 cm for a 1-keV plasma. However, for a magnetic white dwarf, Zheleznyakov, Koryagin, & Serber (2004) note that electron-cyclotron emission lines and radiative losses even more severely constrain the parameters of a hypothesized hot corona.

For the 15-MG field of GD356, we computed the radiative transfer in a hot corona, including cyclotron and bremsstrahlung emissivities and opacities due to cyclotron radiation (Chanmugam et al. 1989) and Faraday rotation and mixing. Figure 3 displays the emergent spectrum for white-dwarf parameters appropriate to GD 356 (§4) and coronal density and temperatures given in the caption. For a density comparable to the upper limit set by the *Chandra* observation, the hypothesized hot corona would emit extremely strong thermal cyclotron lines in the near-infrared band — namely, around the second and third harmonics of the cyclotron frequency ($\nu_B = 42$ THz, $\lambda_B = 7.1$ μm). The JHK photometry (Skrutskie et al. 2006) shows no indication of such an excess, indicating that a hot corona does not exist or has a density much lower than the upper limit set by the X-ray observations. Alternatively,

the magnetic field could be somewhat weaker than 15 MG, which would shift the strong third harmonic ($\nu_3 = 126$ THz, $\lambda_3 = 2.4 \mu\text{m}$) to a lower frequency, longward of the K_s band. Nevertheless, our calculation confirms the conclusion of Zheleznyakov, Koryagin, & Serber (2004): Infrared–visible spectrophotometry is potentially a powerful probe of any hot corona around a magnetic white dwarf.

In addition to producing potentially detectable emission lines, thermal cyclotron radiation would be the dominant cooling mechanism in a hot corona around a magnetic white dwarf. Figure 4 displays the radiated thermal cyclotron and bremsstrahlung luminosity for a supposed isothermal corona around GD 356 ($B = 15$ MG), as a function of density for various electron temperatures between 0.125 keV and 2.0 keV. As the plot clearly shows, cyclotron cooling dramatically exceeds bremsstrahlung cooling for a hot, tenuous plasma above a magnetic white dwarf. Indeed, for GD 356, the coronal thermal cyclotron luminosity rivals the photospheric luminosity unless the electron density is very much less than the upper limit set by the X-ray observation.

Strong cyclotron cooling above a magnetic white dwarf imposes severe demands upon any coronal heating mechanism. As Figure 4 demonstrates, even the weak requirement (Zheleznyakov, Koryagin, & Serber 2004) that the coronal thermal cyclotron luminosity not exceed the photospheric luminosity limits the electron density to $n_0 < 3 \times 10^9 \text{ cm}^{-3}$ for $kT = 1$ keV. If an acoustic flux as large as $10^{10} \text{ erg cm}^{-2} \text{ s}^{-1}$ (Musielak 1987) efficiently heats a corona around GD 356, this heating rate can balance cyclotron cooling for $n_0 \approx 3 \times 10^5 \text{ cm}^{-3}$ for $kT = 1$ keV. This is about 6-orders-of-magnitude less than the density limit set by X-ray non-detection!

For an electron density $n_0 < 3 \times 10^6 \text{ cm}^{-3}$ — approximately independent of temperature — a corona above the white-dwarf photosphere would be transparent to cyclotron radiation in the 15-MG field of GD 356. However, when transparent, the cyclotron cooling time — again approximately independent of temperature — is only $2 \mu\text{s}$ in this magnetic field. For electron densities and temperatures of interest, the mean time between collisions — about $(1.4 \times 10^9 \text{ s cm}^{-3}) (kT/(1 \text{ keV}))^{1.5} n_e^{-1}$ — is much longer than this cyclotron cooling time. Thus, the plasma would not be in local thermodynamic equilibrium (LTE, Zheleznyakov, Koryagin, & Serber 2004, and references therein), unless some collisionless process — e.g., scattering by Alfvén waves — intervenes to transfer energy to the electrons’ transverse degrees of freedom, on this very short timescale.

6.3. Summary

In summary, our *Chandra* observation of the single, cool white dwarf GD 356 limits the luminosity and density of a hypothesized hot corona to $L_X < 6.0 \times 10^{25}$ erg s⁻¹ and $n_0 < 4.4 \times 10^{11}$ cm⁻³ (99.7% confidence), for a 1-keV thermal-bremsstrahlung spectrum. We also re-analyzed archival *ROSAT* data for this white dwarf, G 99-47, GD 90, G 195-19, and WD 2316+123, as well as archival *Chandra* data for LHS 1038 and GD 358, using a statistical methodology (described in the Appendix) better suited to the low-count observations. Our upper limits are reasonably consistent with those of the original authors and lie somewhat above the limits we set for GD 356. As an aside to these searches for X-ray emission from cool white dwarfs, we have listed all *Chandra*-detected sources in the LHS-1038, GD-356, and GD-358 fields on the ACIS-S3 CCD.

We have shown (see also Zheleznyakov, Koryagin, & Serber 2004) that for a magnetic white dwarf (such as GD 356), the non-detection of infrared–visible cyclotron emission lines can more severely constrain the parameters for a hot corona than does an X-ray non-detection. Furthermore, strong cyclotron cooling places extreme demands upon any coronal-heating mechanism. Indeed, our preliminary theoretical analysis suggests that cyclotron cooling around a magnetic white dwarf renders problematic the formation and maintenance of a hot corona. However, we require a more thorough study to prove this conclusively.

Those of us at NASA’s Marshall Space Flight Center (MSFC) acknowledge support from the *Chandra* Program. VEZ acknowledges support from the NASA Postdoctoral Program (NPP). Our analyses utilized software tools from the *Chandra* X-ray Center (operated for NASA by the Smithsonian Astrophysical Observatory, Cambridge MA) and from the High-Energy Astrophysics Science Archive Research Center (HEASARC, operated by the NASA Goddard Space Flight Center, Greenbelt MD, and by the Smithsonian Astrophysical Observatory, Cambridge MA) In addition, our research utilized the SIMBAD database and VizieR catalog access tool (operated at Centre de Données astronomiques de Strasbourg, France) and NASA’s Astrophysics Data System (operated by the Harvard–Smithsonian Center for Astrophysics, Cambridge MA).

A. Statistical Methodology

Statistical estimates of source and background counts and their errors often merely approximately describe an observation or apply only in the large-number limit. Here we present a statistical methodology that more generally describes apertured data (including allowing for uncertainty in the background) and makes no large-number assumption. First (§A.1) we obtain the probability distribution that accurately describes the observation and provides the basis for the statistical analyses to follow. We then describe an appropriate statistical test for detection of a source (§A.2) and one for constraining the expectation value for the number of source events (§A.3).

A.1. Probability for Observed Events

We characterize a measurement (realization) in terms of the observed number of events (counts) m_T and m_R in disjoint regions (apertures) T and R of known measure (solid-angle, area, wavelength band, time interval, etc., as appropriate) Ω_T and Ω_R , respectively. We regard T as a “Target” aperture that *may* contain a source with an expectation value \bar{m}_S events (counts); R as a “Reference” aperture that contains *no* source. Although no source lies within R , source events may occur in R if their distribution is not delta-distributed — i.e., confined to a point. Thus, we define Ψ_T and Ψ_R to be the known fractions of source events in the Target T and Reference R apertures, such that the expectation values for the number of source events are $\bar{m}_S\Psi_T$ and $\bar{m}_S\Psi_R$, respectively. In addition to source events, apertures T and R contain background (non-source) events, with expectation values $\bar{\mu}_B\Omega_T$ and $\bar{\mu}_B\Omega_R$, with $\bar{\mu}_B$ the expectation value for the density (per unit measure) of background events. For convenience, we denote with a subscripted “ U ” parameters or values over the combined aperture $U \equiv T \cup R$, with $T \cap R = 0$ — namely, $\Omega_U = \Omega_T + \Omega_R$, $\Psi_U = \Psi_T + \Psi_R$, and $m_U = m_T + m_R$.

Consequently, the expectation values for the number of events (counts) in apertures T and R are \bar{m}_T and \bar{m}_R , respectively:

$$\bar{m}_T = \bar{m}_S\Psi_T + \bar{\mu}_B\Omega_T, \quad (\text{A1})$$

$$\bar{m}_R = \bar{m}_S\Psi_R + \bar{\mu}_B\Omega_R. \quad (\text{A2})$$

Hence, the probability for m_T and m_R events in an observation (realization) is

$$P_{m_T, m_R}(\bar{m}_T, \bar{m}_R) = [\bar{m}_T^{m_T} e^{-\bar{m}_T} / m_T!] \times [\bar{m}_R^{m_R} e^{-\bar{m}_R} / m_R!]. \quad (\text{A3})$$

Upon substituting Equations A1 and A2 into Equation A3,

$$P_{m_T, m_R}(\bar{m}_S, \bar{\mu}_B; \Psi_T, \Psi_R, \Omega_T, \Omega_R) = [(\bar{m}_S\Psi_T + \bar{\mu}_B\Omega_T)^{m_T} e^{-(\bar{m}_S\Psi_T + \bar{\mu}_B\Omega_T)} / m_T!] \times$$

$$[(\bar{m}_S \Psi_R + \bar{\mu}_B \Omega_R)^{m_R} e^{-(\bar{m}_S \Psi_R + \bar{\mu}_B \Omega_R)} / m_R!]. \quad (\text{A4})$$

Given values for the known parameters (Ψ_T , Ψ_R , Ω_T , and Ω_R) and for the observed number of events (m_T and m_R) in each aperture, Equation A4 provides the basis for statistical tests to constrain expectation values for source events (\bar{m}_S) and for background event density ($\bar{\mu}_B$).

A.2. Detection of a Source

The first type of statistical test addresses detection. Note that this is a test for *detection* only: It provides neither a measured value nor an upper limit. In order to test for detection of a source in the target aperture T , we investigate the hypothesis that there is *no source* — i.e., that $\bar{m}_S = 0$. Under this null hypothesis, the conditional probability of obtaining m_T and m_R (background) events in apertures T and R , given $m_U \equiv m_T + m_R$ events in both apertures, is

$$P_{m_T, m_R}(0, \bar{\mu}_B; \Omega_T, \Omega_R | m_U) = P_{m_T, m_R}(0, \bar{\mu}_B; \Omega_T, \Omega_R) / P_{m_U}(0, \bar{\mu}_B; \Omega_U), \quad (\text{A5})$$

with $\Omega_U \equiv \Omega_T + \Omega_R$. From the Poisson distribution (Equation A4), the conditional probability (Equation A5) reduces to the obvious binomial distribution, independent of $\bar{\mu}_B$ under the null hypothesis:

$$\begin{aligned} P_{m_T, m_R}(\Omega_T, \Omega_R | m_U; \bar{m}_S = 0) &= P_{m_T, m_R}(\Omega_T, \Omega_R) / P_{m_U}(\Omega_U) \\ &= \left(\frac{\Omega_T^{m_T}}{m_T!} \right) \left(\frac{\Omega_R^{m_R}}{m_R!} \right) / \left(\frac{\Omega_U^{m_U}}{m_U!} \right) \\ &= \frac{m_U!}{m_T! m_R!} \left(\frac{\Omega_T}{\Omega_U} \right)^{m_T} \left(\frac{\Omega_R}{\Omega_U} \right)^{m_R}. \end{aligned} \quad (\text{A6})$$

The cumulative probability of obtaining m_T or more events in the Target aperture T , given $\bar{m}_S = 0$ and $m_U = m_T + m_R$ events in the combined aperture $\Omega_U = \Omega_T + \Omega_R$ is then

$$\mathcal{P}(\geq m_T | m_U; \bar{m}_S = 0) = \sum_{m=m_T}^{m_U} \frac{m_U!}{m! (m_U - m)!} \left(\frac{\Omega_T}{\Omega_U} \right)^m \left(1 - \frac{\Omega_T}{\Omega_U} \right)^{m_U - m}. \quad (\text{A7})$$

Consequently, Equation A7 gives a confidence level \mathcal{C} for detection of a source — i.e., for showing that $\bar{m}_S > 0$.

$$\begin{aligned} \mathcal{C}(\bar{m}_S > 0 | m_T, m_R; \Omega_T, \Omega_R) &= \mathcal{P}(< m_T | m_U; \bar{m}_S = 0) = 1 - \mathcal{P}(\geq m_T | m_U; \bar{m}_S = 0) \\ &= \sum_{m=0}^{m_T-1} \frac{m_U!}{m! (m_U - m)!} \left(\frac{\Omega_T}{\Omega_U} \right)^m \left(1 - \frac{\Omega_T}{\Omega_U} \right)^{m_U - m}. \end{aligned} \quad (\text{A8})$$

This expression is valid for any number of events, in either the Target or the Reference aperture. Thus, it does not require that the background event density (μ_B) is statistically well determined.

If the expectation value for the background event density is well known, then we can simplify Equation A4 to the more familiar

$$P_{m_T}(0, \mu_B; \Omega_T) = \frac{(\mu_B \Omega_T)^{m_T}}{m_T!} e^{-\mu_B \Omega_T} . \quad (\text{A9})$$

Given μ_B , the corresponding cumulative probability of obtaining m_T or more (background) events in the Target aperture then becomes

$$\mathcal{P}(\geq m_T \mid \mu_B \Omega_T; \bar{m}_S = 0) = \sum_{m=m_T}^{\infty} \frac{(\mu_B \Omega_T)^m}{m!} e^{-\mu_B \Omega_T} . \quad (\text{A10})$$

Therefore, Equation A10 yields a confidence level \mathcal{C} for detection of a source — i.e., for showing that $\bar{m}_S > 0$.

$$\begin{aligned} \mathcal{C}(\bar{m}_S > 0 \mid m_T; \mu_B \Omega_T) &= \mathcal{P}(< m_T \mid \mu_B \Omega_T; \bar{m}_S = 0) = 1 - \mathcal{P}(\geq m_T \mid \mu_B \Omega_T; \bar{m}_S = 0) \\ &= \sum_{m=0}^{m_T-1} \frac{(\mu_B \Omega_T)^m}{m!} e^{-\mu_B \Omega_T} . \end{aligned} \quad (\text{A11})$$

A.3. Measurement of Source

The second type of statistical test addresses measurement of the expectation value \bar{m}_S for the number of source events. Using Equation A4 as a likelihood function for the parameters m_S and μ_B , we obtain maximum-likelihood estimators for each.

$$\hat{m}_S = \frac{m_T \Omega_R - m_R \Omega_T}{\Psi_T \Omega_R - \Psi_R \Omega_T} , \quad (\text{A12})$$

$$\hat{\mu}_B = \frac{m_R \Psi_T - m_T \Psi_R}{\Psi_T \Omega_R - \Psi_R \Omega_T} . \quad (\text{A13})$$

Evaluation of the second-order partial derivatives of these parameters about their maximum-likelihood estimators leads to estimators for the components of the covariance matrix.

$$\hat{\sigma}_{m_S}^2 = \text{covar}(m_S, m_S) = \left(\frac{\Psi_T^2}{m_T} + \frac{\Psi_R^2}{m_R} \right)^{-1} , \quad (\text{A14})$$

$$\hat{\sigma}_{\mu_B}^2 = \text{covar}(\mu_B, \mu_B) = \left(\frac{\Omega_T^2}{m_T} + \frac{\Omega_R^2}{m_R} \right)^{-1} , \quad (\text{A15})$$

$$\hat{\sigma}_{m_S, \mu_B} = \text{covar}(m_S, \mu_B) = \left(\frac{\Psi_T \Omega_T}{m_T} + \frac{\Psi_R \Omega_R}{m_R} \right)^{-1} . \quad (\text{A16})$$

Here, $\hat{\sigma}_{m_S}$ and $\hat{\sigma}_{\mu_B}$ are the maximum-likelihood estimators for the standard deviation in m_S and μ_B ; $\sigma_{m_S, \mu_B} \neq 0$ shows that the estimators for m_S and μ_B are correlated.

Equations A14, A15, and A16 do not accurately describe the probability distribution for m_S and μ_B except in the large-number limit—i.e., when the probability is approximately normally distributed. Thus, to obtain an accurate description of the probability density function for m_S and μ_B , we return to Equation A4.

Equation A4 gives the probability for m_T and m_R events in apertures T and S , given the expectation values \bar{m}_S and $\bar{\mu}_B$ — i.e., $P_{m_T, m_R}(\bar{m}_S, \bar{\mu}_B) = P(m_T, m_R | \bar{m}_S, \bar{\mu}_B)$. From this, one constructs a probability density function describing the (normalized) likelihood for the expectation values, given the observed distribution of events — i.e., $p(m_S, \mu_B | m_T, m_R)$. In order to facilitate this construction, we rewrite Equation A4, after slightly redefining variables and constant coefficients:

$$P(m_T, m_R | \nu_S, \nu_B) = \frac{(\psi_T \nu_S + \omega_T \nu_B)^{m_T}}{m_T!} \frac{(\psi_R \nu_S + \omega_R \nu_B)^{m_R}}{m_R!} e^{-(\nu_S + \nu_B)}. \quad (\text{A17})$$

The new variables are the expectation value for the number of source events in both apertures combined — $\nu_S \equiv \Psi_U m_S = (\Psi_T + \Psi_R) m_S$ — and the expectation value for the number of background events in both apertures combined — $\nu_B \equiv \Omega_U \mu_B = (\Omega_T + \Omega_R) \mu_B$. The new (constant, predetermined) coefficients are the expected fractions of total source events in apertures T and R — $\psi_T \equiv \Psi_T / \Psi_U = \Psi_T / (\Psi_T + \Psi_R)$ and $\psi_R \equiv \Psi_R / \Psi_U = \Psi_R / (\Psi_T + \Psi_R)$, respectively — and the expected fractions of total background events in apertures T and R — $\omega_T \equiv \Omega_T / \Omega_U = \Omega_T / (\Omega_T + \Omega_R)$ and $\omega_R \equiv \Omega_R / \Omega_U = \Omega_R / (\Omega_T + \Omega_R)$, respectively. Thus, $\psi_T + \psi_R = 1$, so that ψ_T or ψ_R is the probability that a given source event occurs in aperture T or R , respectively. Analogously, $\omega_T + \omega_R = 1$, so that ω_T or ω_R is the probability that a given background event occurs in aperture T or R , respectively. Expanding Equation A17 in terms of a double binomial series, we obtain

$$P(m_T, m_R | \nu_S, \nu_B) = \sum_{i=0}^{m_T} \sum_{j=0}^{m_R} \frac{\psi_T^i \psi_R^{m_R-j} \omega_R^j \omega_T^{m_T-j}}{i!(m_R-j)! j!(m_T-i)!} \times \nu_S^{i+m_R-j} \nu_B^{j+m_T-i} e^{-(\nu_S + \nu_B)}. \quad (\text{A18})$$

Dividing Equation A18 by the partition function $Z(m_T, m_R)$ — equivalent to normalizing the (unweighted, cf. Kraft, Burrows, & Nousek 1991) integral of $P(m_T, m_R | \nu_S, \nu_B)$ over all possible values $(0, \infty)$ of ν_S and ν_B — we derive the desired probability density function:

$$p(\nu_S, \nu_B | m_T, m_R) = \frac{P(m_T, m_R | \nu_S, \nu_B)}{Z(m_T, m_R)}$$

$$\begin{aligned}
&= \frac{1}{Z(m_T, m_R)} \sum_{i=0}^{m_T} \sum_{j=0}^{m_R} \frac{\psi_T^i \psi_R^{m_R-j}}{i!(m_R-j)!} \frac{\omega_R^j \omega_T^{m_T-j}}{j!(m_T-i)!} \\
&\quad \times \nu_S^{i+m_R-j} \nu_B^{j+m_T-i} e^{-(\nu_S+\nu_B)}, \tag{A19}
\end{aligned}$$

where the partition function

$$Z(m_T, m_R) = \sum_{i=0}^{m_T} \sum_{j=0}^{m_R} \frac{(i+m_R-j)!}{i!(m_R-j)!} \psi_T^i \psi_R^{m_R-j} \frac{(j+m_T-i)!}{j!(m_T-i)!} \omega_R^j \omega_T^{m_T-i}. \tag{A20}$$

Note that the partition function (Equation A20) is the *a priori* probability that, given $m_U = m_T + m_R$ total (source and background) events, m_T and m_R events occur in apertures T and R , respectively.

We may integrate the probability density $p(\nu_S, \nu_B | m_T, m_R)$ from Equations A19 and A20 to constrain jointly the values of ν_S and ν_B at a specified confidence level \mathcal{C} . Alternatively, we may constrain either parameter individually, after integrating over the other's full range $(0, \infty)$. Thus, the probability density for the expectation value ν_S of the number of source events in the combined aperture ($U \equiv T \cup R$), without regard to the value of ν_B , is

$$\begin{aligned}
p(\nu_S | m_T, m_R) &= \frac{1}{Z(m_T, m_R)} \sum_{i=0}^{m_T} \sum_{j=0}^{m_R} \frac{(j+m_T-i)!}{j!(m_T-i)!} \omega_R^j \omega_T^{m_T-i} \\
&\quad \times \frac{\nu_S^{i+m_R-j} e^{-\nu_S}}{i!(m_R-j)!} \psi_T^i \psi_R^{m_R-j}, \tag{A21}
\end{aligned}$$

For example, to establish an upper limit to the expectation value $\bar{\nu}_S$ (without regard to ν_B) at a confidence level \mathcal{C} , one solves

$$\begin{aligned}
1 - \mathcal{C}(\bar{\nu}_S < \nu_S | m_T, m_R) &= \int_{\nu_S}^{\infty} p(\nu'_S | m_T, m_R) d\nu'_S \\
&= \frac{1}{Z(m_T, m_R)} \sum_{i=0}^{m_T} \sum_{j=0}^{m_R} \frac{(j+m_T-i)!}{j!(m_T-i)!} \omega_R^j \omega_T^{m_T-i} \\
&\quad \times \frac{\Gamma(i+m_R-j+1, \nu_S)}{i!(m_R-j)!} \psi_T^i \psi_R^{m_R-j}, \tag{A22}
\end{aligned}$$

where $\Gamma(n+1, \nu)$ is the (upper) incomplete gamma function.

In the special case that $\psi_T \rightarrow 1$ and $\psi_R \rightarrow 0$ — i.e., the expected fraction of source events in the reference aperture is negligible — the double sum reduces to the single sum

$$1 - \mathcal{C}(\bar{\nu}_S < \nu_S | m_T, m_R) \xrightarrow{\psi_R \rightarrow 0} \frac{1}{Z(m_T, m_R)} \sum_{i=0}^{m_T} \frac{(m_R+m_T-i)!}{m_R!(m_T-i)!} \omega_R^{m_R} \omega_T^{m_T-i}$$

$$\begin{aligned}
 & \times \frac{\Gamma(i+1, \nu_S)}{i!} \\
 = & \frac{1}{Z(m_T, m_R)} \sum_{k=0}^{m_T} \frac{(m_R+k)!}{m_R! k!} \omega_R^{m_R} \omega_T^k \\
 & \times \frac{\Gamma(m_T-k+1, \nu_S)}{(m_T-k)!}, \tag{A23}
 \end{aligned}$$

The partition function also reduces to a single sum — namely,

$$\begin{aligned}
 Z(m_T, m_R) & \xrightarrow{\psi_R \rightarrow 0} \sum_{i=0}^{m_T} \frac{(m_R+m_T-i)!}{m_R! (m_T-i)!} \omega_R^{m_R} \omega_T^{m_T-i} \\
 & = \sum_{k=0}^{m_T} \frac{(m_R+k)!}{m_R! k!} \omega_R^{m_R} \omega_T^k. \tag{A24}
 \end{aligned}$$

REFERENCES

- Arnaud, K. A., Zheleznyakov, V. V., & Trimble, V. 1992, *PASP*, 104, 239
- Bespalov, P. A., & Zheleznyakov, V. V. 1990, *Sov. Astron. Lett.*, 16, 442
- Barstow, M. A., et al. 1993, *MNRAS*, 264, 16
- Boese, F.G. 2000, *A&A Suppl. Ser.*, 141, 507
- Böhm, K. H., & Cassinelli, J. 1971, *A&A*, 12, 21
- Cavallo, R., Arnaud, K. A., Trimble, V. 1993, *J. Astrophys. Astron.*, 14, 141
- Chanmugam, G., Barrett, P. E., Wu, K., & Courtney, M. W. 1989, *ApJS*, 71, 323
- Ferrario, L., Wickramasinghe, D. T., Liebert, J., Schmidt, G. D., & Beiging, J. H. 1997, *MNRAS* 289, 105
- Fleming, T. A., Werner, K., & Barstow, M. A. 1993, *ApJ*, 416, L79
- Fontaine, G., Montmerle, T., & Michaud, G. 1982, *ApJ*, 257, 695
- Greenstein, J. L., & McCarthy, J. K. 1985, *ApJ*, 289, 732
- Jordan, S. 2001, *ASPC*, 226, 269
- Kahn, S. M., Wesmael, F., Liebert, J., Raymond, J. C., Steiner, J. E., Shipman, H. L. 1984, *ApJ*, 278, 255

- Kawaler, S., Sekii, T., & Gough, D., 1999, *ApJ*, 516, 349
- Kidder, K. M., Holberg, J. B., Barstow, M. A., Tweedy, R. W., & Wesmael, F. 1992, *ApJ*, 394, 288
- Koester, D. 2002, *A&A Rev.*, 11, 33
- Koester, D., Beuermann, K., Thomas, H.-C., Graser, U., Giommi, P., & Tagliaferri, G. 1990, *A&A*, 239, 260
- Kraft, R. P., Burrows, D. N. & Nousek, J. A. 1991, *ApJ*, 374, 344
- Li, J., Wickramasinghe, D. T., Ferrario, L. 1998, *ApJ*, 503, L151
- McCook, G. P., & Sion, E. M. 1999, *ApJS*, 121, 1
- Mermilliod, J.-C., & Mermilliod, M. 1994, *Catalog of Mean UBV Data on Stars* (New York: Springer-Verlag)
- Mewe, R., Heise, J., Gronenschild, E. H. B. M., Brinkman, A. C., Schrijver, J., & den Boggende, A. J. F., 1975, *Nature*, 256, 711
- Monet, D. G., et al. 2003, *AJ*, 125, 984
- Musielak, Z. E. 1987, *ApJ*, 322, 234
- Musielak, Z. E., & Fontenla, J. M. 1989, *ApJ*, 346, 435
- Musielak, Z. E., Porter, J. G., & Davis, J. M., 1995, *ApJ*, 453, L33
- Musielak, Z.E., Noble, M., Porter, J. G. & Winget, D. E. 2003, *ApJ*, 593, 481
- Musielak, Z. E., Winget, D. E., & Montgomery, M. H. 2005, *ApJ*, 630, 506
- Ochsenbein, F., Bauer P., & Marcout, J. 2000, *A&AS*, 143, 221
- Paerels, F. B. S., & Heise, J. 1989, *ApJ*, 339, 1000
- Petre, R., Shipman, H. L., & Canizares, C. R. 1986, *ApJ*, 304, 356
- Provencal, J. L., Shipman, H. L., & MacDonald, J. 2005, *ApJ*, 627, 418
- Schmidt, G. D., & Smith, P. S. 1995, *ApJ*, 448, 305
- Serber, A. V. 1990, *Sov. Astron.*, 34, 291

- Shipman, H. L. 1976, *ApJ*, 206, L67
- Skrutskie, M. F., et al. 2006, *AJ*, 131, 1163
- Tennant, A. F. 2006, *AJ*, 132, 1372
- Thomas, J. H., Markiel, J. A., & Van Horn, H. M. 1995, *ApJ*, 453, 403
- van Altena, W. F., Lee, J. T., & Hoffleit, E. D. 1995, *The General Catalogue of Trigonometric Stellar Parallaxes*, (4th ed.; New Haven CT: Yale University Observatory)
- Wesmael, F., Auer, L. H., Van Horn, H. M., & Savedoff, M. P. 1980, *ApJS*, 43, 159
- Winget, D. E. et al., 1994, *ApJ*, 430, 839
- Zheleznyakov, V. V., Koryagin, S. A., & Serber, A. V. 2004, *Astron. Reports*, 31, 143
- Zheleznyakov, V. V., & Litvinchuk, A. A. 1984, *Ap&SS*, 105, 73
- Zheleznyakov, V. V., Serber, A. V., & Kuijpers, J. 1996, *A&A*, 308, 465

Table 1. General properties of of GD 356 and other single white dwarfs.

(1)	(2)	(3)	(4)	(5)	(6)	(7)	(8)	(9)
Name	RA(J2000) ^a h m s	Dec(J2000) ^a ° ' "	μ_N ^b "/y	μ_W ^b "/y	D ^c pc	Spectral type ^d	T_{eff} ^e K	B ^e MG
LHS 1038	00 12 14.80	+50 25 21.4	−0.456	−0.548	11.0	DA8	6400	0.09
G 99-47	05 56 25.47	+05 21 48.6	−0.446	−0.918	8.0	DAP9	5600	27
GD 90	08 19 46.38	+37 31 28.1	−0.112	−0.100	50	DAH5	11000	10
G 195-19	09 15 56.23	+53 25 24.9	−1.080	−1.116	10.3	DCP7	8000	100
GD 356	16 40 57.16	+53 41 09.6	−0.118	−0.186	21.1	DAH	7500	14
GD 358	16 47 18.39	+32 28 32.9	−0.166	+0.026	36.6	DBV2	24000	0.0013
2316+123	23 18 45.10	+12 36 02.9	+0.102	−0.010	40	DAP	11800	56

Note. —

^a J2000 coordinates are from the 2MASS All-Sky Catalog of Point Sources (Skrutskie et al. 2006) for epoch 2000.00.

^b J2000 proper-motion components μ_N and μ_W are from the Whole-Sky USNO-B1.0 Catalog (Monet et al. 2003).

^c Distances are from the Yale Catalog of Trigonometric Parallaxes (van Altena, Lee, & Hoffleit 1995), except (non-parallax) estimates for GD 90 and 2316+123 (Musielak, Porter, & Davis 1995).

^d Spectral types are from the Villanova Catalog of Spectroscopically Identified White Dwarfs (McCook & Sion 1999).

^e Surface effective temperatures and magnetic fields are from Jordan (2001) and references therein, except for GD 358 (Winget et al. 1994).

Table 2. X-ray observations of GD 356 and other single white dwarfs.

(1)	(2)	(3)	(4)	(5)	(6)	(7)	(8)	(9)	(10)	(11)	(12)
Name	Obs. ^a	Epoch ^b $t_{\text{obs}} - 2000$	Time ks	m_T ^c	Ω_T ^c "/2	m_R ^c	Ω_R ^c "/2	C_{det} ^d %	\bar{m}_S ^e	$\log[L_X]$ ^f (cgs)	$\log[n_0]$ ^g (cgs)
LHS 1038	<i>Chandra</i>	+0.97	5.88	0	3.14	2,029	234,000	0	<5.0	<25.95	<11.72
G 99-47	<i>ROSAT</i>	−7.75	9.28	44	25,500	85	45,200	30	<23.4	<26.21	<11.85
GD 90	<i>ROSAT</i>	−7.75	8.56	91	25,500	157	45,200	57	<40.0	<28.07	<12.78
G 195-19	<i>ROSAT</i>	−7.69	6.99	90	25,500	195	45,200	5	<23.9	<26.57	<12.03
GD 356	<i>Chandra</i>	+5.39	31.8	0	3.14	5,437	216,000	0	<5.0	<25.78	<11.64
GD 356	<i>ROSAT</i>	−7.99	28.2	234	25,500	413	45,200	52	<60.5	<26.99	<12.24
GD 358	<i>Chandra</i>	+1.79	4.88	0	3.14	2,402	233,000	0	<5.0	<27.06	<12.28
2316+123	<i>ROSAT</i>	−8.08	9.12	44	25,500	61	45,200	88	<37.7	<27.83	<12.66

Note. —

^a *Chandra* observations used the ACIS-S instrument; *ROSAT* observations used the PSPC.

^b Proper-motion adjustment of coordinates requires epoch of X-ray observation relative to epoch of catalogued position.

^c X-ray observation detected m_T and m_R events in Target T and Reference R apertures, of measure Ω_T and Ω_R , respectively.

^d Source-detection confidence is the probability that the background contributes fewer than the observed number of events in the Target aperture. (Equation A8)

^e Upper limit to the expectation value of 0.1–2.4-keV source events is at (3- σ) 99.7% confidence. (Equation A22)

^f Calculated X-ray luminosity assumes thermal bremsstrahlung at $kT = 1$ keV.

^g Calculated electron density at coronal base assumes thermal bremsstrahlung at $kT = 1$ keV, from a fully ionized plasma with $n_{\text{He}}/n_{\text{H}} = 0.1$, above an opaque white dwarf of radius $0.0105 R_{\odot} = 7.34 \times 10^8$ cm and surface gravity $\log[g(\text{cgs})] = 8$.

Table 3. *Chandra*-detected sources in the GD-356 field.

(1)	(2)	(3)	(4)	(5)	(6)
Source	RA(J2000) h m s	Dec(J2000) ° ' "	θ_{ext}^a "	m_D^b	θ_{99}^c "
1	16 40 45.029	+53 44 47.38	2.7	8.9	1.25
2	16 40 45.299	+53 45 13.15	3.1	13.6	1.18
3	16 40 53.706	+53 44 42.50	2.4	9.2	1.15
4	16 40 55.545	+53 40 25.24	1.3	22.0	0.69
5	16 40 56.104	+53 39 18.33	1.7	25.9	0.73
6	16 40 59.258	+53 41 59.41	1.2	36.4	0.66
7	16 41 00.438	+53 42 03.31	1.3	10.2	0.78
8	16 41 04.242	+53 40 20.98	1.6	7.3	0.94
9	16 41 05.997	+53 43 18.82	2.0	21.0	0.80
10	16 41 06.757	+53 37 52.85	3.3	30.6	0.94
11	16 41 07.650	+53 45 27.75	3.7	17.8	1.23
12	16 41 10.745	+53 44 36.43	3.2	16.5	1.13
13	16 41 13.050	+53 41 57.24	2.2	12.9	0.97
14	16 41 14.806	+53 41 41.18	2.4	12.6	1.02
15	16 41 15.481	+53 44 10.91	3.4	4559.0	0.61
16	16 41 16.876	+53 42 56.29	2.9	118.6	0.69
17	16 41 19.134	+53 44 11.29	3.9	32.1	1.03
18	16 41 21.033	+53 40 54.25	3.3	17.6	1.13
19	16 41 24.066	+53 41 48.86	3.8	8.2	1.71
20	16 41 30.445	+53 41 18.79	5.0	27.8	1.30
21	16 41 32.519	+53 36 40.09	8.4	17.8	2.49
22	16 41 33.184	+53 43 05.51	5.9	12.7	2.10
23	16 41 37.639	+53 39 57.65	6.9	8.5	2.93

Note. —

^a The extraction radius demarks the detect cell for collecting X-ray counts.

^b An ACIS-S3 observation (ObsID 4484) acquired these detect-cell counts in 31.8 ks.

^c This radius encloses the true position of the detected source at 99% confidence.

Table 4. *Chandra*-detected sources in the LHS-1038 field.

(1)	(2)	(3)	(4)	(5)	(6)
Source	RA(J2000) h m s	Dec(J2000) ° ' "	θ_{ext}^a "	m_D^b	θ_{99}^c "
1	0 12 05.742	+50 28 17.79	2.8	11.3	1.16
2	0 12 08.128	+50 30 16.70	4.6	10.1	1.86
3	0 12 10.118	+50 28 30.63	2.7	60.9	0.73
4	0 12 31.360	+50 32 16.93	8.1	35.5	1.75

Note. —

^a The extraction radius demarks the detect cell for collecting X-ray counts.

^b An ACIS-S3 observation (ObsID 1864) acquired these detect-cell counts in 5.88 ks.

^c This radius encloses the true position of the detected source at 99% confidence.

Table 5. *Chandra*-detected sources in the GD-358 field.

(1)	(2)	(3)	(4)	(5)	(6)
Source	RA(J2000) h m s	Dec(J2000) ° ' "	θ_{ext}^a "	m_D^b	θ_{99}^c "
1	16 46 55.620	+32 29 49.17	4.8	6.9	2.29
2	16 46 58.650	+32 29 30.20	3.9	9.6	1.64
3	16 47 07.418	+32 30 50.62	3.0	25.1	0.95
4	16 47 08.044	+32 25 17.23	2.7	17.2	0.99
5	16 47 13.515	+32 32 03.03	3.5	20.6	1.12
6	16 47 17.610	+32 33 15.56	4.8	25.3	1.31
7	16 47 18.628	+32 27 51.63	1.1	51.1	0.63
8	16 47 18.645	+32 29 16.22	1.4	13.3	0.76
9	16 47 26.652	+32 27 30.17	1.4	8.4	0.85
10	16 47 27.949	+32 27 37.51	1.5	13.0	0.80

Note. —

^a The extraction radius demarks the detect cell for collecting X-ray counts.

^b An ACIS-S3 observation (ObsID 1865) acquired these detect-cell counts in 4.88 ks.

^c This radius encloses the true position of the detected source at 99% confidence.

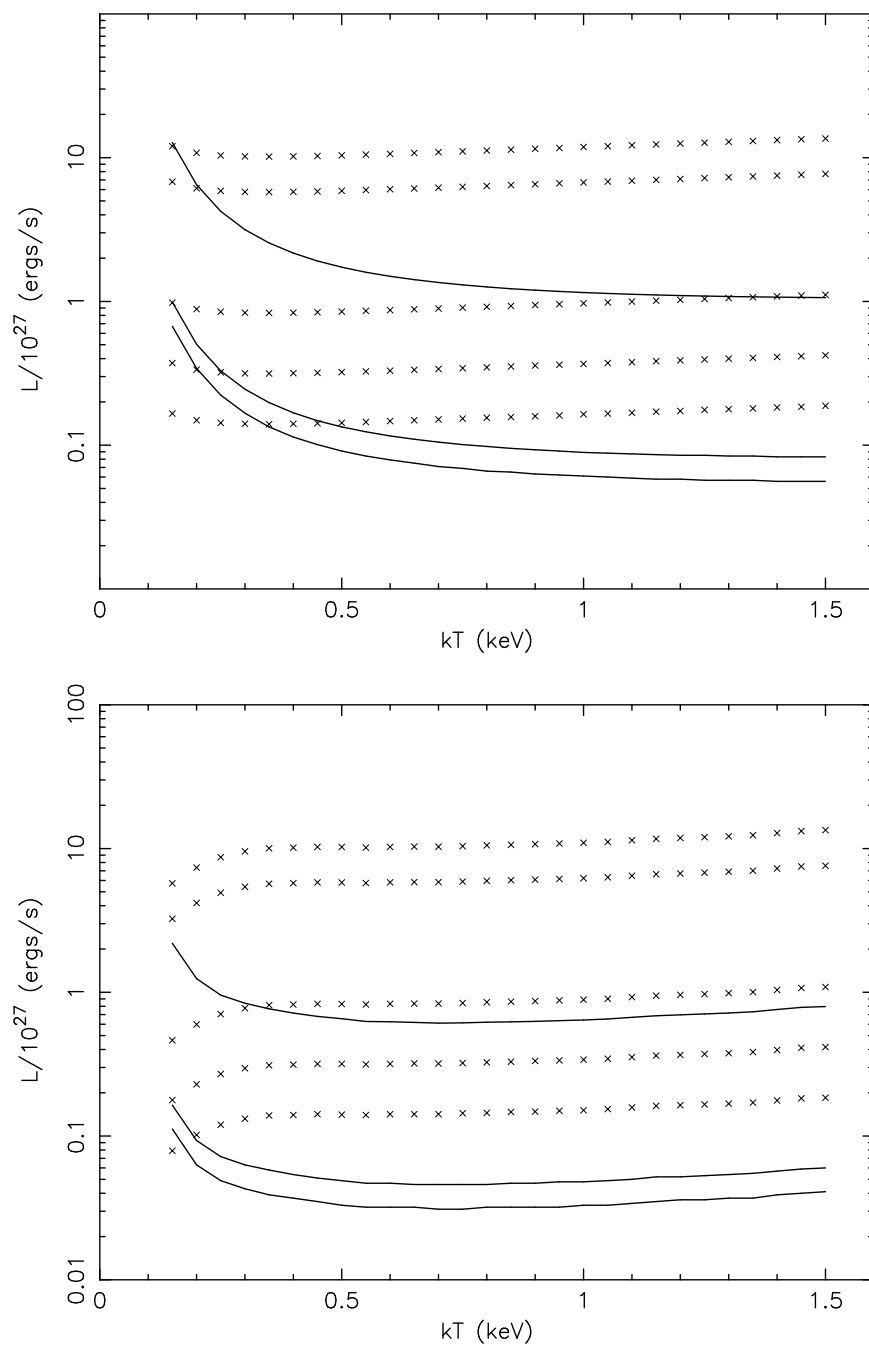


Fig. 1.— The 99.7%-confidence upper limits to total X-ray luminosity versus temperature (upper panel) for bremsstrahlung and (lower panel) for MEKAL models. From lowest to highest, limits based upon *Chandra* data (solid lines) are for GD 356, LHS 1038, and GD 358; those based upon *ROSAT* data (\times markers) are for G 99-47, G 195-19, GD 356, 2316+123, and GD 90.

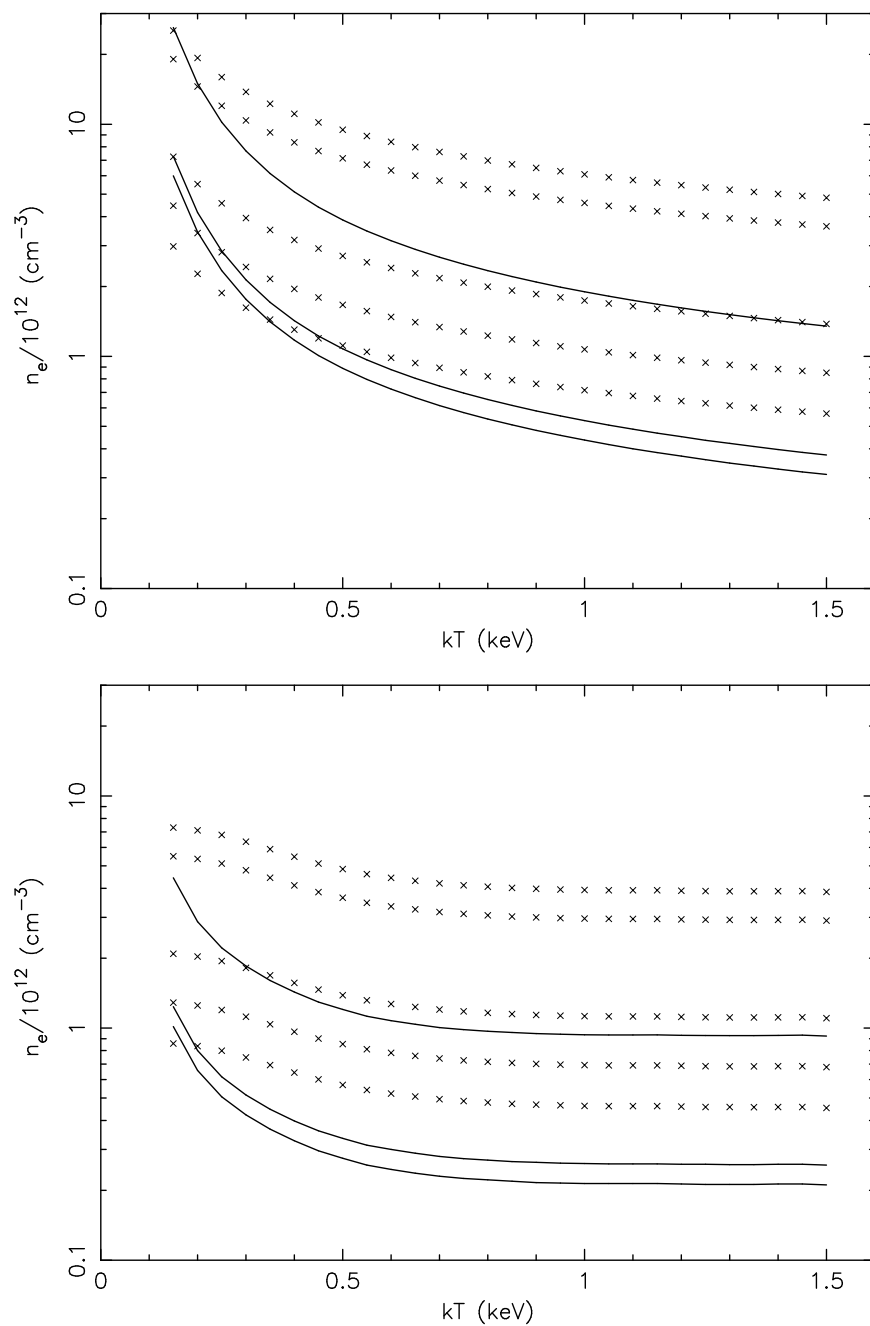


Fig. 2.— The 99.7%-confidence upper limits to coronal electron density versus temperature (upper panel) for bremsstrahlung and (lower panel) for MEKAL models. From lowest to highest, limits based upon *Chandra* data (solid lines) are for GD 356, LHS 1038, and GD 358; those based upon *ROSAT* data (\times markers) are for G 99-47, G 195-19, GD 356, 2316+123, and GD 90.

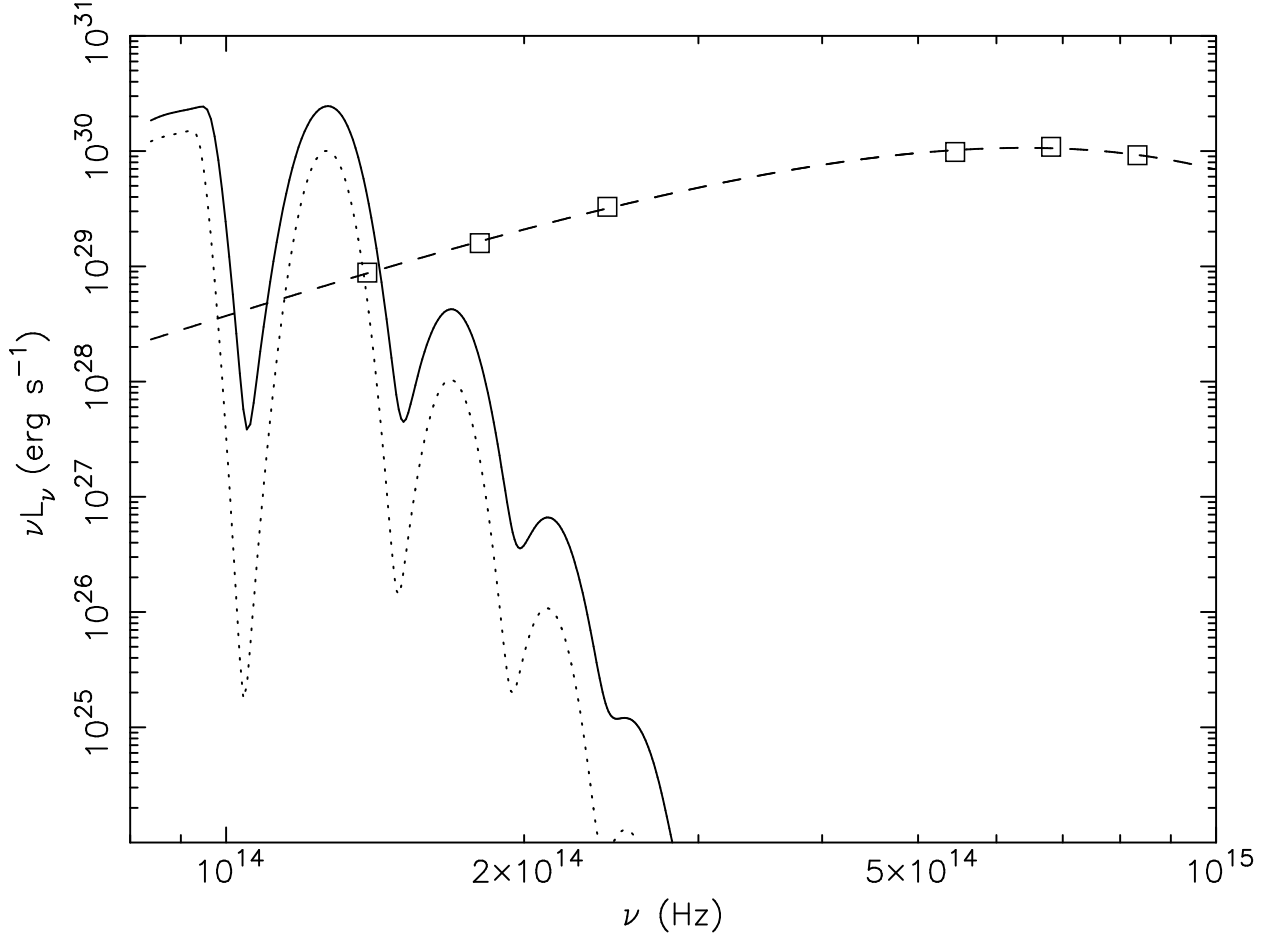


Fig. 3.— Emergent cyclotron spectrum from a hypothesized hot corona around GD 356, in comparison to a 7840-K photospheric spectrum (dashed line) and photometric data (square markers). Calculations assume a 15-MG field at a mean viewing angle $\theta = \arctan(0.5) = 26.6^\circ$ and coronal parameters discussed in the text (§4), for a (coronal-base) electron density $n_0 = 1 \times 10^{11} \text{ cm}^{-3}$ and temperature $T = 1.5 \text{ keV}$ (solid line) or 1.0 keV (dotted line).

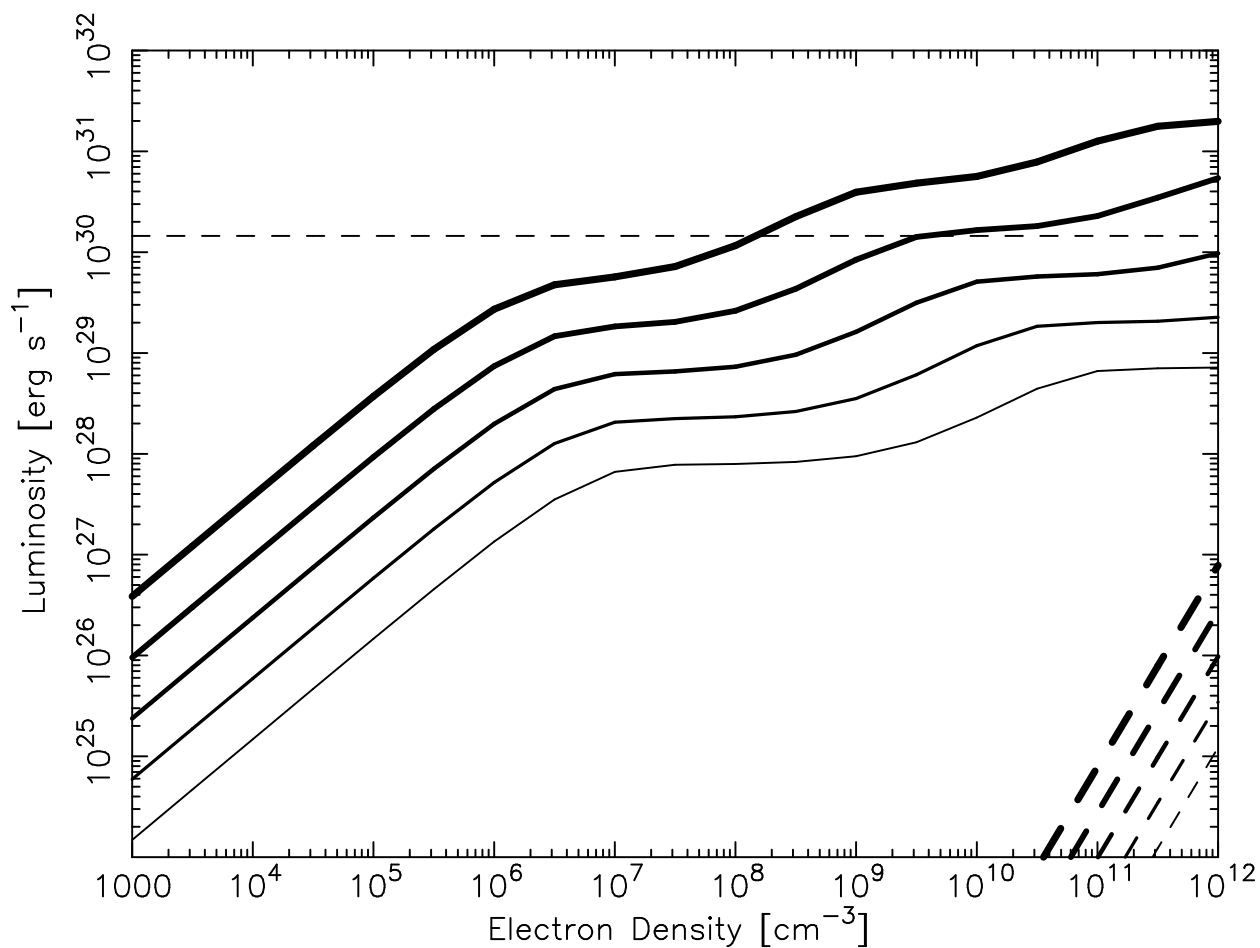


Fig. 4.— Contributors to the luminosity of a hypothetical corona around the magnetic white dwarf GD 356, in comparison to its photospheric luminosity (horizontal, thin dashed line). Solid lines denote the thermal cyclotron luminosity for $B = 15$ MG and $kT = 0.125, 0.25, 0.5, 1.0,$ and 2.0 keV, in increasing thickness. Dotted lines denote the thermal-bremsstrahlung luminosity for the same set of coronal temperatures.